Local phase shift due to interactions in an atom interferometer

Zhibin Yao, Cyrille Solaro, Corentin Carrez, Pierre Cladé, and Saïda Guellati-Khelifa

Phys. Rev. A **106**, 043312 — Published 14 October 2022

DOI: 10.1103/PhysRevA.106.043312

Local phase shift due to interactions in an atom interferometer

Zhibin Yao,[1] Cyrille Solaro,[1] Corentin Carrez,[1] Pierre Cladé,[1] and Saïda Guellati-Khelifa[1, 2, *]

[1] *Laboratoire Kastler Brossel, Sorbonne Université, CNRS, ENS-PSL, Collège de France, 4 place Jussieu, 75005 Paris, France*

[2] *Conservatoire National des Arts et Métiers, 292 rue Saint Martin, 75003 Paris, France*

(Dated: September 19, 2022)

We study the phase shift induced by atomic interactions at the output of an atom interferometer. Due to the mutual interaction between the two overlapping Bose-Einstein condensates, the phase exhibits a spatial profile. We evaluate the phase gradient using a perturbative method based on the Feynman path integral approach. Our model accounts for the effects of the population imbalance between the two arms of the interferometer and the difference between the scattering lengths of the hyperfine levels. We also investigate these effects experimentally by measuring the interaction phase shift for a set parameters. Our experimental results are well reproduced by our theoretical model.

I. INTRODUCTION

Matter-wave interferometry has been used to measure with extreme accuracy several physical quantities [1] such as gravity [2–7], inertial forces [8–11] and fundamental constants [12–14] enabling advanced tests of general relativity [15–18] and quantum electrodynamics [13, 14]. In addition, many experiments based on atom interferometry are underway or have been proposed in order to test short-range forces [19–22] and different models of particle physics in the search for unknown forces or dark energy [23–29]. This technology, which has not yet reached its full potential, is also at the heart of large-scale or space instruments [30–32]. These instruments are being built, with targeted significantly improved performances, for testing fundamental physics with unprecedented accuracy, detecting gravitational waves [33–36] and mapping the Earth's gravitational field from satellites [37, 38].

Both the sensitivity and accuracy of the most advanced atom interferometers are limited by the transverse motion of the atomic cloud [39], which exalts systematic effects related to short-scale intensity fluctuations [40], the Gouy phase, and wavefront curvature [41]. Due to wavefront distortions, transverse motion also limits the diffraction order of large momentum beam splitters [42–45]. In this context, Bose-Einstein condensates (BEC) constitute ideal atomic sources. In addition, the atomic interactions that are inherent in such dense clouds can generate spin squeezing, which could be exploited to surpass the standard quantum limit [46–48].

However, atomic interactions also induce a detrimental phase shift that can undermine the benefits of using Bose-Einstein condensates for precision measurements with atom interferometry. Effects of interactions have been studied both theoretically and experimentally to understand their impact on the phase of Bose-Einstein condensates during free evolution [49–53]. Early work showed that upon release from the trapping potential, the BEC expands due to repulsive interactions and develops a non-uniform phase profile [54–56]. In ref [49], the authors measured the functional form and time evolution of this phase profile by combining interferometry with spatially resolved auto-correlation. They also measured the small velocity imparted to the two BEC wave-packets from their mutual repulsion. More recent work has focused on the local modification of the condensate phase due to mutual interactions and shows that modifications occur only in the region where the wave packets overlap [53].

This non-uniform phase profile impacts the accuracy of measurements based on atom interferometry. In this paper, we experimentally evaluate this effect by measuring locally the phase shift at the output port of an atom interferometer and its dependence upon the population imbalance, the trapping potential frequencies and the condensate release time. Furthermore, we present a new approach to calculate the effect of interactions using the Feynman path integral. Numerical simulation based on this method reproduces well our experimental data. This approach differs from that used in previous works [50–53] where the evolution of the BEC phase is obtained from the GP equation by considering the time evolution of its density. In most works the expansion of the condensate is described by the Castin and Dum model [57] valid in Thomas Fermi regime. Our method based on the Feynman path integral allows to calculate the phase shift at the output of the interferometer for any geometry. It also allows the contributions of the self and mutual interactions to be evaluated separately.

The paper is organized as follows. Section II presents the theoretical model we have developed to evaluate the phase shift at the output of an atomic interferometer formed by a sequence of three light pulses in the so-called Mach-Zehnder configuration (see Fig. 1). Each pulse induces a stimulated Raman transition. We use a perturbation approach to derive a general formula for calculating the effects of self-interaction and mutual interaction between the two interfering condensates. Finally, based on Castin Dum's description of the BEC wave function, we obtain a formula for the phase profile, the signature of the mutual interaction. In Sect. III we present a set of

* guellati@lkb.upmc.fr

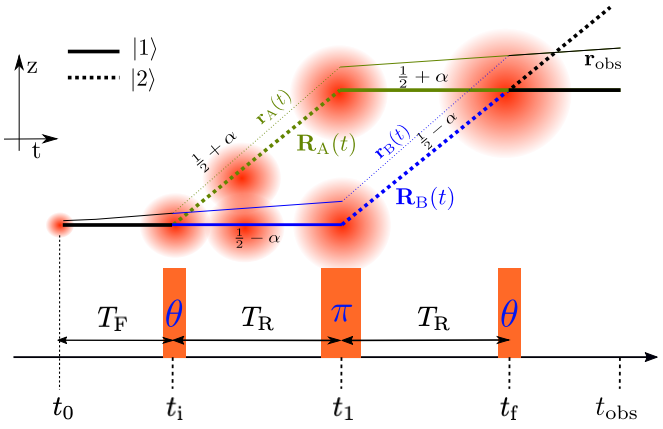

FIG. 1. At time t_0 we release the BEC from the dipole optical trap. During the free fall time, it expands and the interaction energy decreases. After a falling time T_F, we apply the three pulses sequence $\theta - \pi - \theta$. In green, trajectory A and blue trajectory B. Solid line state $|1\rangle$, dashed line state $|2\rangle$. Thick line : trajectories $R_{A/B}$ of the center of mass of the atomic wave packet. Thin line : trajectory $r_{A/B}$ used to integrate the Lagragian for a given final position $\boldsymbol{r}_{\rm obs}$.

experimental results. We study the behavior of both the phase gradient and the total interaction phase shift by varying different experimental parameters.

II. THEORETICAL EVALUATION OF THE INTERACTION PHASE SHIFT

The goal of this section is to calculate the phase at the output of an atom interferometer in the mean field approximation using the Feynman path integral method [58]. Here, we apply this approach, which is commonly used in atom interferometry to calculate the phase induced by external potential, to the case of the mean field. The Feynman path integral method states that, given an initial wave packet with phase $\phi(\boldsymbol{r}(t_0), t_0)$ at time t_0, the phase at time t can be calculated by integrating the Lagrangian $\mathcal{L}$ along the classical trajectory $\boldsymbol{r}(t)$ that makes the action extremal:

$$\phi(\boldsymbol{r}(t), t) - \phi(\boldsymbol{r}(t_0), t_0) = \frac{1}{\hbar}\int_{t_0}^{t} \mathcal{L}\left(\dot{\boldsymbol{r}}(t), \boldsymbol{r}(t), t\right) \mathrm{d}t \quad (1)$$

with

$$\mathcal{L}\left(\dot{\mathbf{r}}(t), \mathbf{r}(t), t\right) = \frac{1}{2} m \dot{\mathbf{r}}^2(t) - V(\mathbf{r}, t) \quad (2)$$

V being the potential experienced by an atom of mass m. The trajectory should match the initial velocity of the cloud ($\dot{\boldsymbol{r}}(t_0) = -i(\hbar\nabla\phi/m)$).

In the mean-field approximation, the interaction potential is proportional to the cloud density $\rho(\boldsymbol{r}, t)$. To calculate the phase in our interferometer, we have to consider the internal states and the effect of the Raman transition. The Raman transition couples two internal states, namely $|1\rangle$ and $|2\rangle$. The total mean field experienced by an atom in state $|i\rangle$ is the sum of the mean field induced by the atoms in state $|i\rangle$ from its own atomic cloud (the so-called self-interaction) and the one induced by the atoms from the other cloud (the so-called mutual interaction) (see Figure 1). It can be written as:

$$V_{\rm MF}(\boldsymbol{r}, t, i) = \sum_j N g_{ij} \rho(\boldsymbol{r}, t, j) \quad (3)$$

with $g_{ij} = 4\pi\hbar^2 a_{ij}/m$, where a_{ij} are the scattering lengths. The interaction potential depends on the normalized density $\rho(\boldsymbol{r}, t, j)$ of the atoms in the internal states $|j\rangle$.

Raman transitions are performed with two counter-propagating laser beams ($\boldsymbol{k}_1, \omega_1$ and $\boldsymbol{k}_2, \omega_2$), leading to an effective momentum $\boldsymbol{k}_{\rm eff} = \boldsymbol{k}_1 - \boldsymbol{k}_2$ and pulsation $\omega = \omega_1 - \omega_2$ [59]. To use the Lagrangian formalism, one can take into account the effect of the Raman transitions with an effective potential. For the three pulses interferometer in Figure 1, this potential is given for each path A and B by [60]:

$$W_A(\boldsymbol{r}, t) = \hbar\left(\boldsymbol{k}_{\rm eff}\cdot\boldsymbol{r}(t) - \omega t\right)\left(\delta(t - t_i) - \delta(t - t_1)\right) \quad (4)$$

$$W_B(\boldsymbol{r}, t) = \hbar\left(\boldsymbol{k}_{\rm eff}\cdot\boldsymbol{r}(t) - \omega t\right)\left(\delta(t - t_1) - \delta(t - t_{\rm f})\right) \quad (5)$$

Indeed, when an atom performs a Raman transition and is transferred from $|1\rangle$ to $|2\rangle$, the effective phase of the laser is added to the phase of its wave function. It is subtracted when the atom is transferred from state $|2\rangle$ to state $|1\rangle$. With this effective potential, the trajectory that extremizes the action, accounts for the recoil induced by each Raman transition.

To compute the phase difference at a given observation position $\boldsymbol{r}_{\rm obs}$ and time $t_{\rm obs}$ (see figure1), we consider two trajectories $\boldsymbol{r}_A(t)$ and $\boldsymbol{r}_B(t)$ which start with the initial velocity $\boldsymbol{v}_0$ of the cloud and satisfy $\boldsymbol{r}_A(t_{\rm obs}) = \boldsymbol{r}_B(t_{\rm obs}) = \boldsymbol{r}_{\rm obs}$ (note that they may not start at the same position). The spatially dependent phase difference between the two waves is given by :

$$\Delta\phi(\boldsymbol{r}_{\rm obs}) = \phi(\boldsymbol{r}_A(t_0), t_0) - \phi(\boldsymbol{r}_B(t_0), t_0) + \frac{1}{\hbar}\int_{t_0}^{t_{\rm obs}} \left(\mathcal{L}_{\mathcal{A}}(\dot{\boldsymbol{r}}_A, \boldsymbol{r}_A, t) - \mathcal{L}_{\mathcal{B}}(\dot{\boldsymbol{r}}_B, \boldsymbol{r}_B, t)\right) dt \quad (6)$$

In typical experiments, the Thomas-Fermi approximation is applicable and the Castin-Dum description of the BEC density [57] is commonly used. However, due to the mutual interaction, it is not possible to compute analytically the density in each branch of the interferometer and therefore the classical trajectories which depend on the interaction potential. We propose here to treat the mutual interaction as a perturbation.

Let us now consider a reference configuration where: i) there is no interaction between the two clouds, and ii) the mean field is the same on both arms of the interferometer (same scattering length $g_{11} = g_{22}$ and a 50/50

atomic beam splitter). In this situation, the two clouds are identical with respect to their center of mass and have the same density $\rho_{\rm ref}(\boldsymbol{r},t)$. The reference potential used to calculate the classical trajectories is

$$V_{\rm ref,A/B}(\boldsymbol{R}_{A/B}(t)+\boldsymbol{r},t)=c_{\rm ref}(t)Ng_{11}\rho_{\rm ref}(\boldsymbol{r},t) \quad (7)$$

where $\boldsymbol{R}_{A/B}$ are the trajectories of the centers of mass (thick lines of Fig. 1) and

$$c_{\rm ref}(t)=\begin{cases}1 & t<t_i\\ \frac{1}{2} & t_i\le t\le t_{\rm obs}\end{cases} \quad (8)$$

Assuming that the shape of the cloud is given by this reference density, the potential due to the atomic interactions felt by the atoms in the cloud along the trajectory A, for $t_i<t<t_f$, is:

$$V_A(\boldsymbol{R}_A(t)+\boldsymbol{r},t)=N\frac{g_{11}}{2}\rho_{\rm ref}(\boldsymbol{r},t)+N\left(c_A(t)g_{\xi_A(t),\xi_A(t)}-\frac{g_{11}}{2}\right)\rho_{\rm ref}(\boldsymbol{r},t)+Nc_B(t)g_{\xi_A(t),\xi_B(t)}\rho_{\rm ref}(\boldsymbol{r}+\Delta\boldsymbol{R},t) \quad (9)$$

where $\xi_{A/B}(t)$ represents the internal state of the atom (1 or 2), $c_{A/B}(t)$ is the proportion of atoms in the path A or B and $\Delta\boldsymbol{R}(t)=\boldsymbol{R}_A(t)-\boldsymbol{R}_B(t)$. The first term corresponds to the reference potential, the second to the correction of the self-interaction due to the difference in the scattering lengths a_{11} and a_{22}, and the last term to the mutual interaction. For trajectory B, there is a similar equation, exchanging A and B and replacing $\Delta\boldsymbol{R}(t)$ by $-\Delta\boldsymbol{R}(t)$.

For rubidium, $|(a_{22}-a_{11})/a_{11}|$ is around 6% and in a typical experiment, the population imbalance is a few percent. Moreover, the mutual interaction term is non negligible only when the two clouds overlap. Our approximation consists in considering the last two terms of equation 9 as perturbations when we derive the equations of motion for the classical trajectories. This means that only the first term of equation 9 is responsible for the repulsive force. We denote by $V^{\rm pert}_{\rm A/B}$ the interaction potential that accounts for the last two terms.

We now consider an atom after the first Raman pulse. It is in a superposition of two wave packets that propagate along the reference trajectories $\boldsymbol{r}_A$ and $\boldsymbol{r}_B$. These trajectories are determined from the reference configuration. Due to symmetry, the relative trajectories with respect to the motion of the center of mass are the same: we can write $\boldsymbol{r}_{A/B}(t)=\boldsymbol{R}_{A/B}(t)+\boldsymbol{r}_{\rm ref}(t)$. In the absence of any perturbation, the two trajectories are symmetric, and the total phase shift at the output of the interferometer is zero. At first order, the total phase shift could be calculated by integrating the perturbation along the unperturbed trajectories [58]. These trajectories overlap for $t<t_i$ and $t>t_f$ and the potential is the same (atoms are in the same state), we can therefore restrict the integral to $t_i<t<t_f$ and

$$\Delta\phi(\boldsymbol{r}_{\rm obs})=\frac{1}{\hbar}\int_{t_i}^{t_f}\left(V_A^{\rm pert}(\boldsymbol{R}_A(t)+\boldsymbol{r}_{\rm ref}(t),t)-V_B^{\rm pert}(\boldsymbol{R}_B(t)+\boldsymbol{r}_{\rm ref}(t),t)\right)dt \quad (10)$$

By separating contributions from mutual and self-interaction, we obtain

$$\Delta\Phi^{\rm sef}(\boldsymbol{r}_{\rm obs})=\frac{1}{\hbar}N\alpha\left(g_{11}+g_{22}\right)\int_{t_{\rm i}}^{t_{\rm f}}\rho_{\rm ref}(\boldsymbol{r},t)\ {\rm d}t+\frac{1}{\hbar}\frac{N}{2}\delta g\left[\int_{t_{\rm i}}^{t_1}\rho_{\rm ref}(\boldsymbol{r},t)\ {\rm d}t-\int_{t_1}^{t_{\rm f}}\rho_{\rm ref}(\boldsymbol{r},t)\ {\rm d}t\right] \quad (11)$$

$$\begin{aligned}\Delta\Phi^{\rm mut}(\boldsymbol{r}_{\rm obs})=&\frac{1}{\hbar}Ng_{21}\left(\frac{1}{2}-\alpha\right)\left[\int_{t_{\rm i}}^{t_{\rm s}^A}\rho_{\rm ref}(\boldsymbol{r}+\Delta\boldsymbol{R}(t),t)\ {\rm d}t+\int_{t_{\rm c}^A}^{t_{\rm f}}\rho_{\rm ref}(\boldsymbol{r}+\Delta\boldsymbol{R}(t),t)\ {\rm d}t\right]\\&-\frac{1}{\hbar}Ng_{12}\left(\frac{1}{2}+\alpha\right)\left[\int_{t_{\rm i}}^{t_{\rm s}^B}\rho_{\rm ref}(\boldsymbol{r}-\Delta\boldsymbol{R}(t),t)\ {\rm d}t+\int_{t_{\rm c}^B}^{t_{\rm f}}\rho_{\rm ref}(\boldsymbol{r}-\Delta\boldsymbol{R}(t),t)\ {\rm d}t\right]\end{aligned} \quad (12)$$

where $\alpha=|c_A(t)-c_B(t)|/2$ is the population imbalance between the two arms of the interferometer and $\delta g=g_{22}-g_{11}$. The boundaries of the integrals (11) and (12) account for the finite extension of the two interfering clouds: $t_{\rm s}^A$ (resp. $t_{\rm s}^B$) is the separation time when the atom on trajectory A (resp. B) leaves the overlap zone and $t_{\rm c}^A$ (resp. $t_{\rm c}^B$) is the recombination time when the atom on trajectory A (resp. B) enters the overlap zone. They depend on the expansion and the separation velocities of the two interfering condensates.

The Castin-Dum model [57] provides a good description of the BEC dynamics in time-dependent traps when

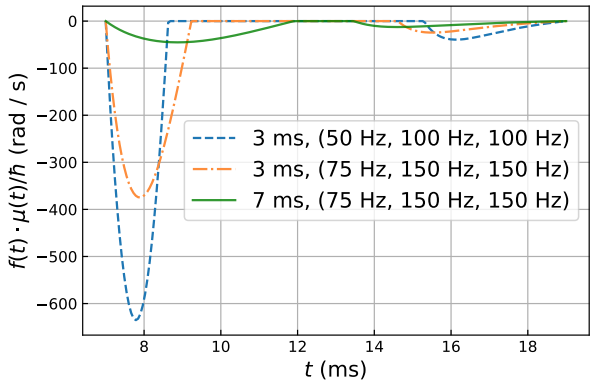

FIG. 2. Evolution of the quantity $f(\Delta Z_{\mathrm{R}})\mu(t)$ during the interferometer sequence for different values of the release time T_{F} and trapping frequencies.

the Thomas Fermi approximation is satisfied. It gives the following formula for the BEC density at time t,

$$\rho(\mathbf{r},t) = \frac{\mu}{g_{11}\lambda_x(t)\lambda_y(t)\lambda_z(t)} \times \left(1 - \sum_{s=x,y,z} \left(r_s(t)/r_{\mathrm{sl}}\lambda_s(t)\right)^2\right) \quad (13)$$

when the last term is positive and $\rho(\mathbf{r},t) = 0$ otherwise. μ denotes the chemical potential of the initial state, i.e., of the system before the application of the first Raman light pulse.

$$\mu = \frac{\hbar\bar{\omega}}{2}\left(15Na\sqrt{\frac{m\bar{\omega}}{\hbar}}\right)^{\frac{2}{5}} \quad \text{with} \quad \bar{\omega} = (\omega_x\omega_y\omega_z)^{\frac{1}{3}}, \quad (14)$$

ω_s is the optical trap frequency along the s axis, $r_{\mathrm{sl}} = \sqrt{2\mu/m\omega_s^2}$ is the Thomas-Fermi radius and the scaling factor $\lambda_s(t)$ is governed by differential equations derived by Castin and Dum from the scaling ansatz for a single component BEC [57]:

$$\frac{\mathrm{d}^2\lambda_s(t)}{\mathrm{d}t^2} = \frac{\omega_s^2}{\lambda_s(t)\lambda_x(t)\lambda_y(t)\lambda_z(t)} \quad (15)$$

In our experiment, the Raman beams propagate along the z-axis. The two clouds hence separate along this direction leading to a phase gradient from the mutual interaction. We obtain the spatial profile of the phase shift $\Delta\Phi^{\mathrm{mut}}(z)$ by averaging equation 12 over transverse coordinates (x, y).

For $\alpha = 0$ (perfect $\pi/2$ Raman pulses), we show that the phase $\Delta\Phi^{\mathrm{mut}}$ can be written in first order in z, as

$$\Delta\Phi^{\mathrm{mut}}(z_{\mathrm{obs}}) = \frac{2}{\hbar}\frac{a_{12}}{2a_{11}}\frac{z_{\mathrm{obs}}}{\lambda_z(t_{\mathrm{obs}})}\int_{t_{\mathrm{i}}}^{t_{\mathrm{f}}}\mu(t)f(\Delta Z_{\mathrm{R}})\mathrm{d}t \quad (16)$$

with

$$\mu(t) = \frac{\mu}{\lambda_x(t)\lambda_y(t)\lambda_z(t)}, \quad \Delta Z_{\mathrm{R}} = \frac{\Delta Z}{z_l\lambda_z(t)}, \quad (17)$$

and the function f is defined by

$$f(x) = \begin{cases} x\left(x^4-1\right) & \text{if } x < 1 \\ 0 & \text{otherwise} \end{cases} \quad (18)$$

The form of equation 16 is interesting as it dissociates the effects of the chemical potential $\mu(t)$ and of the separation of the two condensates $f(\Delta Z_{\mathrm{R}})$. The temporal evolution of these two terms depends on the expansion dynamics of the condensate, which is set by the trap frequencies. In figure 2 we plot $\mu(t)f(\Delta Z_{\mathrm{R}})$ for two sets of trapping frequencies and two different release times T_{F}. We clearly observe that the mutual interaction is significant at the beginning of the interferometer and that it declines as the condensates dilute.

III. EXPERIMENT

We produce a rubidium-87 Bose-Einstein condensate by evaporative cooling in an all-optical trap which consists of three Gaussian laser beams at a wavelength of 1070 nm. Two relatively wide beams of 170 μm waist cross under a shallow angle and provide a large trapping volume, the so-called *reservoir*, which is loaded from an optical molasse. A tightly focused third beam of 25 μm waist, the so-called *dimple beam*, crosses the reservoir at an angle of 65°. This geometry provides the high confinement necessary for an efficient evaporation. The maximum laser power in the reservoir and in the dimple is 24 W and 0.5 W, respectively. To produce a BEC in a pure Zeeman state, we use the spin distillation technique [61] where we apply a magnetic field gradient during evaporation that selectively reduces the depth of the trap for magnetically sensitive states. We produce about 220 000 atoms in $|\mathrm{F}=1,\mathrm{m_F}=0\rangle$ after 1.7 s of evaporation. The trapping frequencies (ν_x,ν_y,ν_z) at the end of the evaporation were measured to be (50(2), 115(10), 115(10)) Hz. At time t_0, the BEC is released by turning

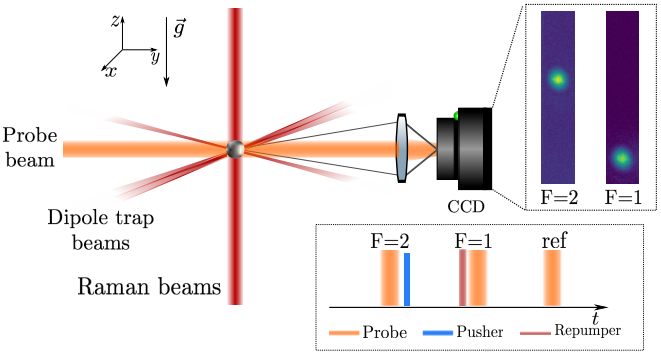

FIG. 3. An overview of the experimental setup. The bottom insert shows the detection timing sequence.

off the trapping potential and falls freely for a duration T_{F} prior we apply the light pulses sequence $\theta - \pi - \theta$ (figure 1). Each light pulse consists of two vertically counter-propagating laser beams, which drive Raman transitions

between the two hyperfine levels $|F = 1, m_F = 0\rangle$ (state $|1\rangle$) and $|F = 2, m_F = 0\rangle$ (state $|2\rangle$) of the $5S_{1/2}$ electronic ground state. The two Raman lasers are phase-locked. A detailed description of the electronic system for controlling their frequencies and their phase difference is given in the supplementary material of reference [14]. The first light pulse splits the initial Bose-Einstein condensate into two wave packets. The relative atom number between the two arms (i.e the parameter α) is controlled by adjusting the duration of the first light pulse. The figure 3 gives an overview of the experimental setup. To measure the number of atoms in $F = 2$ and $F = 1$, we use a sequence of three probe laser pulses, each resonant with the cycling transition ($^5S_{1/2}\ F = 2 \longrightarrow {}^5P_{3/2}\ F' = 3$). The first pulse measures the number of atoms in $F = 2$, which are then pushed away (pusher beam). The atoms in $F = 1$ are first pumped to $F = 2$, then detected by the second probe pulse. The third pulse shines on the camera without atoms to get a reference picture of the laser beam intensity.

To probe the atomic phase, we scan the phase difference of the Raman lasers $\Delta\phi_{\rm L}$ at the third light pulse. We measure by absorption imaging and for different values of $\Delta\phi_{\rm L}$, the number of atoms in each of the two hyperfine states $F = 1$ and $F = 2$ at the end of the interferometer sequence. The top of figure 4 shows the absorption images (yz plane) of the atomic cloud in $F = 1$ taken 33 ms after release from the trap, for a set of $\Delta\phi_{\rm L}$ values. We clearly observe a shift in the center position of the imaged cloud which reveals that the phase is not spatially uniform. To obtain the phase at the z position, we integrate the 2D absorption image, along the y dimension. Then, for each position z, which corresponds to a camera pixel, we calculate the number of atoms as a function of the laser phase $\Delta\Phi_{\rm L}$ and fit those data with a cosine function to extract the atomic phase. This phase is plotted in the bottom of figure 4 for different values of the pulse area θ. For $\theta = \pi/2$, we measure a phase gradient of 3.6 mrad/μm after 7 ms of a fall time of a BEC with an initial atomic density of 4.3×10^{14} atoms/cm^3.

The simulation based on our model fits the experimental data without any adjustment. These theoretical curves were obtained as follows: we first consider an atom at an initial position $\mathbf{r}(t_0)$ and calculate, for all times t between t_0 and $t_{\rm obs}$, the expansion parameters $\lambda_s(t)$ by numerically solving the equation (15) and subsequently the coordinates $r_s(t) = r_s(0)\lambda_s(t)$ $(s = x, y, z)$. We then determine the reference trajectories A and B that account for the effect of the Raman transitions. Finally, we calculate the accumulated phase shift $\Delta\Phi_{\rm at}$ using equations (11) and (12).

At time t after the overlap of the wave packets, the probability $P(F = 1)$ of detecting the atom in $|F = 1\rangle$ at position $\boldsymbol{r}$ is

$$P(F=1) = \frac{\mu - \frac{1}{2}\sum m\omega_s^2 r_s^2(0)}{g_{11} N \lambda_x(t)\lambda_y(t)\lambda_z(t)} \left(\frac{1}{4} - \alpha^2\right) \left|1 + \mathrm{e}^{j(\Delta\Phi_{\rm at} + \Delta\phi_{\rm L})}\right|^2 \tag{19}$$

We repeat this calculation for initial positions on a 3D grid to construct the image of the atomic cloud at the detection time $t_{\rm obs}$. Subsequently, we integrate over the xy dimensions to obtain the total number of atoms at position z. To extract the atomic phase shift, we add a laser phase $\Delta\phi_{\rm L}$ in equation (19) to probe the atomic phase and analyze the simulated images the exact same way we do with the experimental ones.

To evaluate the contribution of the mutual interaction we measured the interaction phase shift as a function of the condensate release time, the trapping frequency ν_z and the population imbalance α. Figure 5 shows the variation of the phase gradient as a function of the release time $T_{\rm F}$. We see that the phase gradient decreases with the release time and becomes almost undetectable after 20 ms. As expected, this is also the case of the total phase shift that accounts for both the mutual and self interaction, even if the population imbalance between the two branches of the interferometer is significant (see figure 6). We measure a total interaction phase shift of (0.49 ± 0.03) rad for an atomic density in an initial BEC of 4.3×10^{14}atoms/cm^3, when $T_F = 4$ ms and $\theta = 0.3\ \pi$.

Finally, we looked at the behavior of the phase shift due to atomic interactions when varying the vertical trapping frequency ν_z. As shown in Figure 7, the phase first increases with the trapping frequency, passes a maximum, and then decreases. This behaviour results from the dependence of the chemical potential, BEC size and expansion rate on trapping frequencies.

The mean field μ scales as $\bar{\omega}^{7/5}$, it increases faster than the size of the condensate, which varies almost linearly with the trapping frequency. Therefore, considering the overlap duration of the two condensates, the contribution of the self-interaction is larger than the mutual interaction.

For a low trapping frequency, the expansion of the atomic cloud is slow and the two BECs rapidly separate after the first Raman pulse (with relative velocity $2v_r$). The main contribution to the total phase shift $\Delta\phi$ comes from the self-interaction which increases rapidly as the trapping frequency increases. At a high trapping frequency, the expansion of the cloud dominates due to the repulsive potential and therefore the self-interaction decreases since both BECs are diluted.

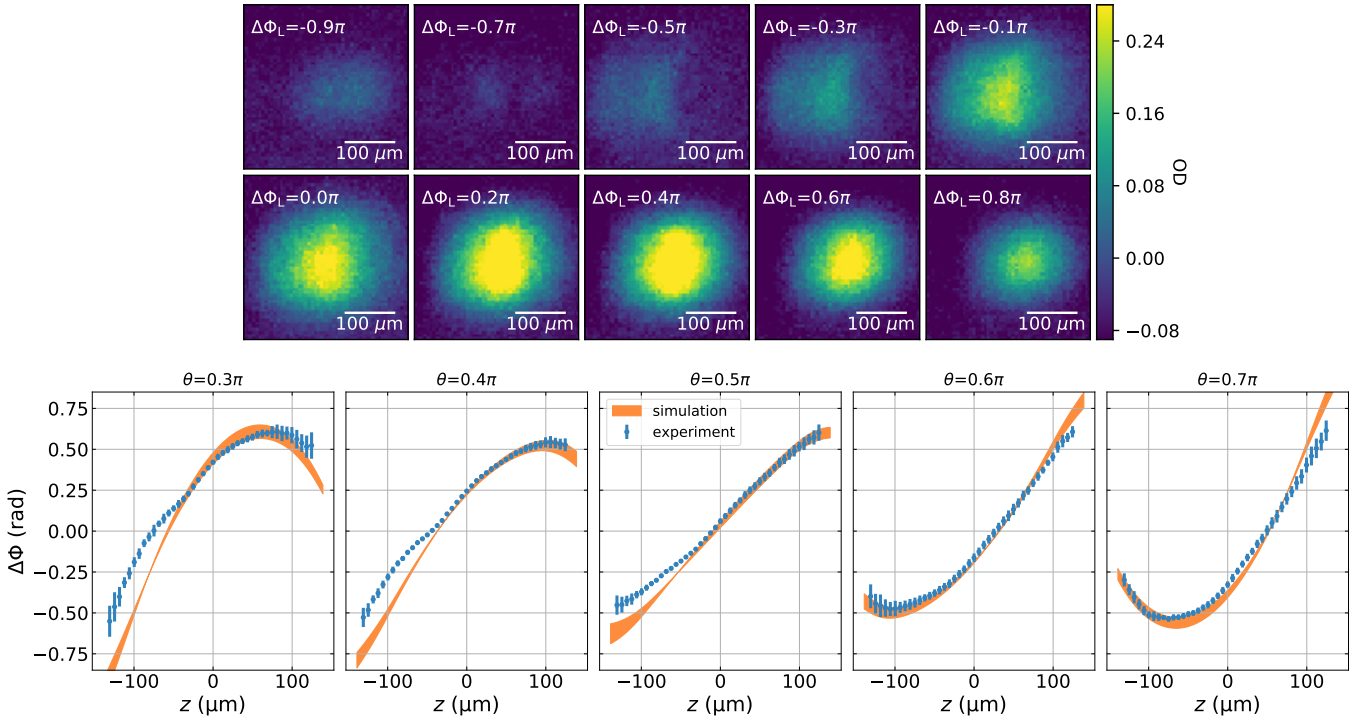

FIG. 4. Top: absorption pictures obtained by scanning from $-\pi$ to π, the phase difference $\Delta\Phi_{\mathrm{L}}$ between the two Raman laser at the last pulse. Optical densities greater than 0.25 have been saturated. The experimental parameters are $T_{\mathrm{R}} = 6$ ms, $T_{\mathrm{F}} = 7$ ms and $\theta = 0.3\pi$. Bottom: Variation of the phase shift at the output of the interferometer along the vertical z axis, for different Raman pulse area θ. The shaded area accounts for the fluctuation of the pulse area and trapping frequencies.

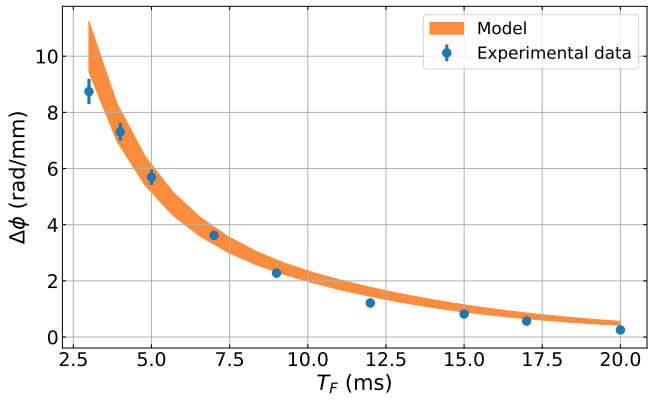

FIG. 5. Phase gradient as function of release time t_F. The orange shaded curve is the range of calculated phase gradient accounting for the uncertainty on the trapping frequencies.

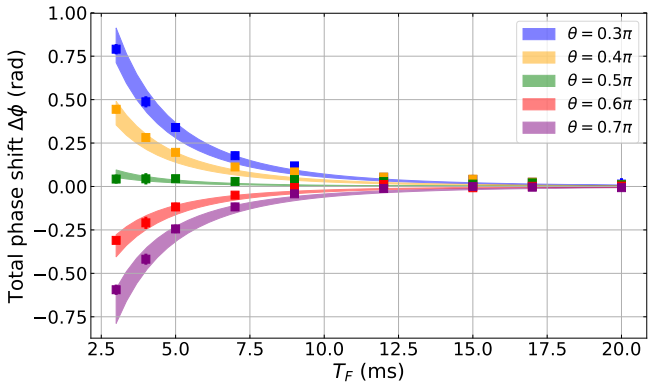

FIG. 6. Total phase shift accounting for both mutual and self interactions as a function of the release time T_{F}, for different values of the Raman pulse area θ (from 0.3π to 0.7π), with $\mathrm{T_R} = 6$ms. Square points are experimental data. The shaded curve is the range of calculated total interaction phase shift, accounting for uncertainty on the pulse area and the trapping frequencies.

IV. CONCLUSION

In this paper, we have investigated in detail both theoretically and experimentally the phase shift due to atomic interactions in an atom interferometer. Our theoretical model relies on the Feynman integral approach which is used to derive general formulas for phase shifts related to self-interaction and mutual interaction. Our model is general and accounts for the effect of a population imbalance between the two arms of the interferometer as well as of the difference in scattering lengths of the hyperfine states. It allows to evaluate precisely the interaction phase shifts knowing the time evolution of the spatial

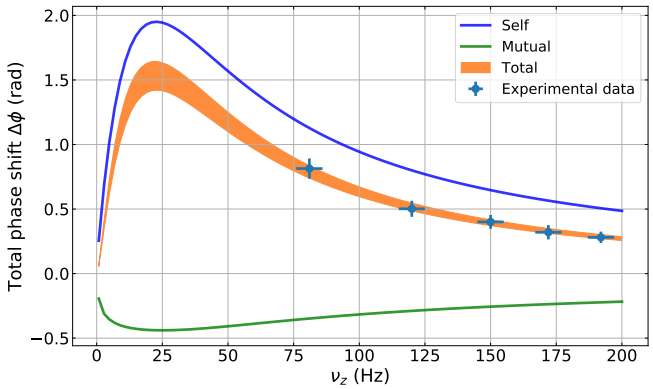

FIG. 7. Variation of interaction phase shift with the vertical trapping frequency ν_z. Parameters are $T_F = 3$ ms, $T_R = 6$ ms and $\theta = 0.35\ \pi$. The shaded orange curve is the range of calculated total interaction phase shift, accounting for uncertainty on the number of atoms and the trapping frequencies. The experimental data set satisfies the Thomas Fermi approximation.

density of the Bose-Einstein condensate. Relying on the Castin-Dum model, which describes the temporal evolution of the BEC spatial density in the Thomas-Fermi regime, we calculated the phase shift induced by the atomic interactions and in particular the phase gradient resulting from the mutual interaction. We measured experimentally the phase gradient and the total phase shift (accounting for mutual and self interactions) by varying the experimental parameters (BEC release time, trapping frequencies and Raman coupling). The theoretical curves reproduce well the experimental data without any adjustment of the parameters. In particular, the work presented in this paper has enabled us to evaluate the phase gradient due to the mutual interactions between the two interfering condensates. It also provides theoretical tools, validated by the experiment, to evaluate the phase shifts induced by atomic interactions. The treatment of the interaction effect by the Feynman path integral approach can be generalized to other atom interferometer configurations and offers a simple way to accurately evaluate the related systematic effect that could affect high-precision measurements with atom interferometry.

ACKNOWLEDGMENTS

This work was supported by the Agence Nationale pour la Recherche TONICS Project-(ANR-21-CE47-0017-01), the US National Institute of Standards and Technology (NIST) Precision Measurement Grant Program under the award number 60NANB16D271 and the LaBEx Cluster of Excellence FIRST-TF (ANR-10-LABX-48-01), within the Programme investissements davenir operated by the French National Research Agency (ANR). C.S. acknowledges support from Region Ile-de-France through the DIM SIRTEQ Fellowship ELUDA.

[1] R. Geiger, A. Landragin, S. Merlet, and F. P. D. Santos, High-accuracy inertial measurements with cold-atom sensors, AVS Quantum Science **2**, 024702 (2020).
[2] Z.-K. Hu, B.-L. Sun, X.-C. Duan, M.-K. Zhou, L.-L. Chen, S. Zhan, Q.-Z. Zhang, and J. Luo, Demonstration of an ultrahigh-sensitivity atom-interferometry absolute gravimeter, Phys. Rev. A **88**, 043610 (2013).
[3] P. Gillot, O. Francis, A. Landragin, F. P. D. Santos, and S. Merlet, Stability comparison of two absolute gravimeters: optical versus atomic interferometers, Metrologia **51**, L15 (2014).
[4] C. Freier, M. Hauth, V. Schkolnik, B. Leykauf, M. Schilling, H. Wziontek, H.-G. Scherneck, J. Müller, and A. Peters, Mobile quantum gravity sensor with unprecedented stability, J. Phys.: Conf. Ser. **723**, 012050 (2016).
[5] Y. Bidel, N. Zahzam, C. Blanchard, A. Bonnin, M. Cadoret, A. Bresson, D. Rouxel, and M. F. Lequentrec-Lalancette, Absolute marine gravimetry with matter-wave interferometry, Nature Communications **9**, 10.1038/s41467-018-03040-2 (2018).
[6] V. Ménoret, P. Vermeulen, N. L. Moigne, S. Bonvalot, P. Bouyer, A. Landragin, and B. Desruelle, Gravity measurements below 10-9 g with a transportable absolute quantum gravimeter, Scientific Reports **8**, 10.1038/s41598-018-30608-1 (2018).
[7] Y. Bidel, N. Zahzam, A. Bresson, C. Blanchard, M. Cadoret, A. V. Olesen, and R. Forsberg, Absolute airborne gravimetry with a cold atom sensor, Journal of Geodesy **94**, 10.1007/s00190-020-01350-2 (2020).
[8] D. Savoie, M. Altorio, B. Fang, L. A. Sidorenkov, R. Geiger, and A. Landragin, Interleaved atom interferometry for high-sensitivity inertial measurements, Science Advances **4**, 10.1126/sciadv.aau7948 (2018).
[9] R. Gautier, M. Guessoum, L. A. Sidorenkov, Q. Bouton, A. Landragin, and R. Geiger, Accurate measurement of the sagnac effect for matter waves, Science Advances **8**, 10.1126/sciadv.abn8009 (2022).
[10] A. Bonnin, C. Diboune, N. Zahzam, Y. Bidel, M. Cadoret, and A. Bresson, New concepts of inertial measurements with multi-species atom interferometry, Applied Physics B **124**, 10.1007/s00340-018-7051-5 (2018).
[11] D. Yankelev, C. Avinadav, N. Davidson, and O. Firstenberg, Multiport atom interferometry for inertial sensing, Phys. Rev. A **100**, 023617 (2019).
[12] G. Rosi, F. Sorrentino, L. Cacciapuoti, M. Prevedelli, and G. M. Tino, Precision measurement of the newtonian gravitational constant using cold atoms, Nature **510**, 518 (2014).
[13] R. H. Parker, C. Yu, W. Zhong, B. Estey, and H. Müller, Measurement of the fine-structure constant as

a test of the Standard Model, Science **360**, 191 (2018), arXiv:1812.04130 [physics.atom-ph].
[14] L. Morel, Z. Yao, P. Cladé, and S. Guellati-Khélifa, Determination of the fine-structure constant with an accuracy of 81 parts per trillion, Nature **588**, 61 (2020).
[15] G. M. Tino, Testing gravity with cold atom interferometry: results and prospects, Quantum Science and Technology **6**, 024014 (2021).
[16] P. Asenbaum, C. Overstreet, M. Kim, J. Curti, and M. A. Kasevich, Atom-interferometric test of the equivalence principle at the 10^{-12} level, Phys. Rev. Lett. **125**, 191101 (2020).
[17] H. Albers, A. Herbst, L. L. Richardson, H. Heine, D. Nath, J. Hartwig, C. Schubert, C. Vogt, M. Woltmann, C. Lmmerzahl, S. Herrmann, W. Ertmer, E. M. Rasel, and D. Schlippert, Quantum test of the universality of free fall using rubidium and potassium, The European Physical Journal D **74**, 10.1140/epjd/e2020-10132-6 (2020).
[18] B. Barrett, G. Condon, L. Chichet, L. Antoni-Micollier, R. Arguel, M. Rabault, C. Pelluet, V. Jarlaud, A. Landragin, P. Bouyer, and B. Battelier, Testing the universality of free fall using correlated 39k–87rb atom interferometers, AVS Quantum Science **4**, 014401 (2022).
[19] S. Dimopoulos and A. A. Geraci, Probing submicron forces by interferometry of bose-einstein condensed atoms, Phys. Rev. D **68**, 124021 (2003).
[20] P. Wolf, P. Lemonde, A. Lambrecht, S. Bize, A. Landragin, and A. Clairon, From optical lattice clocks to the measurement of forces in the casimir regime, Phys. Rev. A **75**, 063608 (2007).
[21] F. Sorrentino, A. Alberti, G. Ferrari, V. V. Ivanov, N. Poli, M. Schioppo, and G. M. Tino, Phys. Rev. A **79**, 013409 (2009).
[22] X. Alauze, A. Bonnin, C. Solaro, and F. Pereira dos Santos, A trapped ultracold atom force sensor with a μm-scale spatial resolution, New Journal of Physics **20**, 083014 (2018).
[23] P. Hamilton, M. Jaffe, P. Haslinger, Q. Simmons, H. Mller, and J. Khoury, Atom-interferometry constraints on dark energy, Science **349**, 849 (2015).
[24] K. Van Tilburg, N. Leefer, L. Bougas, and D. Budker, Search for ultralight scalar dark matter with atomic spectroscopy, Phys. Rev. Lett. **115**, 011802 (2015).
[25] B. Elder, J. Khoury, P. Haslinger, M. Jaffe, H. Müller, and P. Hamilton, Chameleon dark energy and atom interferometry, Phys. Rev. D **94**, 044051 (2016).
[26] P. W. Graham, D. E. Kaplan, J. Mardon, S. Rajendran, and W. A. Terrano, Dark matter direct detection with accelerometers, Phys. Rev. D **93**, 075029 (2016).
[27] P. W. Graham, D. E. Kaplan, J. Mardon, S. Rajendran, W. A. Terrano, L. Trahms, and T. Wilkason, Spin precession experiments for light axionic dark matter, Phys. Rev. D **97**, 055006 (2018).
[28] P. Haslinger, M. Jaffe, V. Xu, O. Schwartz, M. Sonnleitner, M. Ritsch-Marte, H. Ritsch, and H. Müller, Attractive force on atoms due to blackbody radiation, Nature Physics **14**, 257 (2018).
[29] D. O. Sabulsky, I. Dutta, E. A. Hinds, B. Elder, C. Burrage, and E. J. Copeland, Experiment to detect dark energy forces using atom interferometry, Phys. Rev. Lett. **123**, 061102 (2019).
[30] K. Frye, S. Abend, W. Bartosch, A. Bawamia, D. Becker, H. Blume, C. Braxmaier, S.-W. Chiow, M. A. Efremov, W. Ertmer, P. Fierlinger, T. Franz, N. Gaaloul, J. Grosse, C. Grzeschik, O. Hellmig, V. A. Henderson, W. Herr, U. Israelsson, J. Kohel, M. Krutzik, C. Kürbis, C. Lämmerzahl, M. List, D. Lüdtke, N. Lundblad, J. P. Marburger, M. Meister, M. Mihm, H. Müller, H. Müntinga, A. M. Nepal, T. Oberschulte, A. Papakonstantinou, J. Perovsek, A. Peters, A. Prat, E. M. Rasel, A. Roura, M. Sbroscia, W. P. Schleich, C. Schubert, S. T. Seidel, J. Sommer, C. Spindeldreier, D. Stamper-Kurn, B. K. Stuhl, M. Warner, T. Wendrich, A. Wenzlawski, A. Wicht, P. Windpassinger, N. Yu, and L. Wörner, The bose-einstein condensate and cold atom laboratory, EPJ Quantum Technology **8**, 1 (2021).
[31] D. Aguilera, H. Ahlers, B. Battelier, A. Bawamia, A. Bertoldi, R. Bondarescu, K. Bongs, P. Bouyer, C. Braxmaier, L. Cacciapuoti, C. Chaloner, M. Chwalla, W. Ertmer, M. Franz, N. Gaaloul, M. Gehler, D. Gerardi, L. Gesa, N. Gürlebeck, J. Hartwig, M. Hauth, O. Hellmig, W. Herr, S. Herrmann, A. Heske, A. Hinton, P. Ireland, P. Jetzer, U. Johann, M. Krutzik, A. Kubelka, C. Lämmerzahl, A. Landragin, I. Lloro, D. Massonnet, I. Mateos, A. Milke, M. Nofrarias, M. Oswald, A. Peters, K. Posso-Trujillo, E. Rasel, E. Rocco, A. Roura, J. Rudolph, W. Schleich, C. Schubert, T. Schuldt, S. Seidel, K. Sengstock, C. Sopuerta, F. Sorrentino, D. Summers, G. Tino, C. Trenkel, N. Uzunoglu, W. Von Klitzing, R. Walser, T. Wendrich, A. Wenzlawski, P. Weßels, A. Wicht, E. Wille, M. Williams, P. Windpassinger, and N. Zahzam, Ste-quest - test of the universality of free fall using cold atom interferometry, Classical and Quantum Gravity **31**, 10.1088/0264-9381/31/11/115010 (2014).
[32] D. Becker, M. D. Lachmann, S. T. Seidel, H. Ahlers, A. N. Dinkelaker, J. Grosse, O. Hellmig, H. Müntinga, V. Schkolnik, T. Wendrich, A. Wenzlawski, B. Weps, R. Corgier, T. Franz, N. Gaaloul, W. Herr, D. Lüdtke, M. Popp, S. Amri, H. Duncker, M. Erbe, A. Kohfeldt, A. Kubelka-Lange, C. Braxmaier, E. Charron, W. Ertmer, M. Krutzik, C. Lämmerzahl, A. Peters, W. P. Schleich, K. Sengstock, R. Walser, A. Wicht, P. Windpassinger, and E. M. Rasel, Space-borne bose–einstein condensation for precision interferometry, Nature **562**, 391 (2018).
[33] P. Adamson, S. Chattopadhyay, J. Coleman, P. Graham, S. Geer, R. Harnik, S. Hahn, J. Hogan, M. Kasevich, T. Kovachy, J. Mitchell, R. Plunkett, S. Rajendran, L. Vaerio, and A. Vaspmos, Proposal: P-1101. matter-wave atomic gradiometer interferometric sensor (magis-100) (2018).
[34] A. Arvanitaki, P. W. Graham, J. M. Hogan, S. Rajendran, and K. Van Tilburg, Search for light scalar dark matter with atomic gravitational wave detectors, Phys. Rev. D **97**, 075020 (2018).
[35] B. Canuel, A. Bertoldi, L. Amand, E. Pozzo di Borgo, T. Chantrait, C. Danquigny, M. Dovale Álvarez, B. Fang, A. Freise, R. Geiger, J. Gillot, S. Henry, J. Hinderer, D. Holleville, J. Junca, G. Lefèvre, M. Merzougui, N. Mielec, T. Monfret, S. Pelisson, M. Prevedelli, S. Reynaud, I. Riou, Y. Rogister, S. Rosat, E. Cormier, A. Landragin, W. Chaibi, S. Gaffet, and P. Bouyer, Exploring gravity with the miga large scale atom interferometer, Scientific Reports **8**, 14064 (2018).
[36] M.-S. Zhan, J. Wang, W.-T. Ni, D.-F. Gao, G. Wang, L.-X. He, R.-B. Li, L. Zhou, X. Chen, J.-Q. Zhong,

B. Tang, Z.-W. Yao, L. Zhu, Z.-Y. Xiong, S.-B. Lu, G.-H. Yu, Q.-F. Cheng, M. Liu, Y.-R. Liang, P. Xu, X.-D. He, M. Ke, Z. Tan, and J. Luo, Zaiga: Zhaoshan long-baseline atom interferometer gravitation antenna, International Journal of Modern Physics D **29**, 1940005 (2020), https://doi.org/10.1142/S0218271819400054.

[37] T. Lévèque, C. Fallet, M. Mandea, R. Biancale, J. M. Lemoine, S. Tardivel, S. Delavault, A. Piquereau, S. Bourgogne, F. P. dos Santos, B. Battelier, and P. Bouyer, Gravity field mapping using laser-coupled quantum accelerometers in space, Journal of Geodesy **95**, 1 (2021).

[38] N. Zahzam, B. Christophe, V. Lebat, E. Hardy, P.-A. Huynh, N. Marquet, C. Blanchard, Y. Bidel, A. Bresson, P. Abrykosov, T. Gruber, R. Pail, I. Daras, and O. Carraz, Hybrid electrostatic-atomic accelerometer for future space gravity missions, Remote Sensing **14**, 10.3390/rs14143273 (2022).

[39] A. Louchet-Chauvet, T. Farah, Q. Bodart, A. Clairon, A. Landragin, S. Merlet, and F. Pereira dos Santos, The influence of transverse motion within an atomic gravimeter, New Journal of Physics **13**, 065025 (2011).

[40] S. Bade, L. Djadaojee, M. Andia, P. Cladé, and S. Guellati-Khelifa, Observation of extra photon recoil in a distorted optical field, Phys. Rev. Lett. **121**, 073603 (2018).

[41] A. Wicht, E. Sarajlic, J. M. Hensley, and S. Chu, Phase shifts in precision atom interferometry due to the localization of atoms and optical fields, Phys. Rev. A **72**, 023602 (2005).

[42] P. Cladé, S. Guellati-Khélifa, F. Nez, and F. Biraben, Large momentum beam splitter using bloch oscillations, Phys. Rev. Lett. **102**, 240402 (2009).

[43] H. Müller, S.-w. Chiow, S. Herrmann, and S. Chu, Atom interferometers with scalable enclosed area, Phys. Rev. Lett. **102**, 240403 (2009).

[44] S.-w. Chiow, T. Kovachy, H.-C. Chien, and M. A. Kasevich, $102\hbar k$ large area atom interferometers, Phys. Rev. Lett. **107**, 130403 (2011).

[45] M. Gebbe, J.-N. Siem, M. Gersemann, H. Mntinga, S. Herrmann, C. Lmmerzahl, H. Ahlers, N. Gaaloul, C. Schubert, K. Hammerer, S. Abend, and E. M. Rasel, Twin-lattice atom interferometry, Nature Communications **12**, 2544 (2021).

[46] S. S. Szigeti, S. P. Nolan, J. D. Close, and S. A. Haine, High-precision quantum-enhanced gravimetry with a bose-einstein condensate, Phys. Rev. Lett. **125**, 100402 (2020).

[47] B. K. Malia, J. Martínez-Rincón, Y. Wu, O. Hosten, and M. A. Kasevich, Free space ramsey spectroscopy in rubidium with noise below the quantum projection limit, Phys. Rev. Lett. **125**, 043202 (2020).

[48] M. A. Perlin, C. Qu, and A. M. Rey, Spin squeezing with short-range spin-exchange interactions, Phys. Rev. Lett. **125**, 223401 (2020).

[49] J. E. Simsarian, J. Denschlag, M. Edwards, C. W. Clark, L. Deng, E. W. Hagley, K. Helmerson, S. L. Rolston, and W. D. Phillips, Imaging the phase of an evolving bose-einstein condensate wave function, Phys. Rev. Lett. **85**, 2040 (2000).

[50] A. O. Jamison, J. N. Kutz, and S. Gupta, Atomic interactions in precision interferometry using bose-einstein condensates, Phys. Rev. A **84**, 043643 (2011).

[51] A. O. Jamison, B. Plotkin-Swing, and S. Gupta, Advances in precision contrast interferometry with yb bose-einstein condensates, Phys. Rev. A **90**, 063606 (2014).

[52] R. Jannin, P. Cladé, and S. Guellati-Khélifa, Phase shift due to atom-atom interactions in a light-pulse atom interferometer, Phys. Rev. A **92**, 013616 (2015).

[53] A. Burchianti, C. D'Errico, L. Marconi, F. Minardi, C. Fort, and M. Modugno, Effect of interactions in the interference pattern of bose-einstein condensates, Phys. Rev. A **102**, 043314 (2020).

[54] E. W. Hagley, L. Deng, M. Kozuma, M. Trippenbach, Y. B. Band, M. Edwards, M. Doery, P. S. Julienne, K. Helmerson, S. L. Rolston, and W. D. Phillips, Measurement of the coherence of a bose-einstein condensate, Phys. Rev. Lett. **83**, 3112 (1999).

[55] M. Trippenbach, Y. B. Band, M. Edwards, M. Doery, P. S. Julienne, E. W. Hagley, L. Deng, M. Kozuma, K. Helmerson, S. L. Rolston, and W. D. Phillips, Coherence properties of an atom laser, Journal of Physics B: Atomic, Molecular and Optical Physics **33**, 47 (1999).

[56] I. Bloch, T. W. Hänsch, and T. Esslinger, Measurement of the spatial coherence of a trapped bose gas at the phase transition, Nature **403**, 166 (2000).

[57] Y. Castin and R. Dum, Bose-einstein condensates in time dependent traps, Phys. Rev. Lett. **77**, 5315 (1996).

[58] Pippa Storey and Claude Cohen-Tannoudji, The feynman path integral approach to atomic interferometry. a tutorial, J. Phys. II France **4**, 1999 (1994).

[59] M. Cadoret, E. De Mirandes, P. Clade, F. Nez, L. Julien, F. Biraben, and S. Guellati-Khelifa, Atom interferometry based on light pulses: Application to the high precision measurement of the ratio h/m and the determination of the fine structure constant, EUROPEAN PHYSICAL JOURNAL-SPECIAL TOPICS **172**, 121 (2009).

[60] W. P. Schleich, D. M. Greenberger, and E. M. Rasel, A representation-free description of the kasevich-chu interferometer: a resolution of the redshift controversy, New Journal of Physics **15**, 013007 (2013).

[61] A. Couvert, M. Jeppesen, T. Kawalec, G. Reinaudi, R. Mathevet, and D. Guéry-Odelin, A quasi-monomode guided atom laser from an all-optical bose-einstein condensate, EPL (Europhysics Letters) **83**, 50001 (2008).